

Research Paper

Numerical modelling of granular materials with spherical discrete particles and the bounded rolling friction model. Application to railway ballast



Joaquín Irazábal^{a,*}, Fernando Salazar^a, Eugenio Oñate^{a,b}

^aInternational Center for Numerical Methods in Engineering (CIMNE), Barcelona, Spain

^bPolytechnic University of Catalonia (UPC), Barcelona, Spain

ARTICLE INFO

Article history:

Received 12 September 2016

Received in revised form 24 November 2016

Accepted 31 December 2016

Available online 9 January 2017

Keywords:

Discrete element method

Bounded rolling friction model

Rolling resistance torque

Railway ballast

Railway track stability

ABSTRACT

The Discrete Element Method (DEM) was found to be an effective numerical method for the calculation of engineering problems involving granular materials. However, the representation of irregular particles using the DEM is a very challenging issue, leading to different geometrical approaches. This document presents a new insight in the application of one of those simplifications known as rolling friction, which avoids excessive rotation when irregular shaped materials are simulated as spheric particles. This new approach, called the Bounded Rolling Friction model, was applied to reproduce a ballast resistance test.

© 2017 Elsevier Ltd. All rights reserved.

1. Introduction

Traditionally, complex geomechanic problems were addressed using refined constitutive models based on continuum assumptions. Although these models may be accurate in the evaluation of the critical state of soils [1–4], or the flow of bulk material masses [5], they are not able to represent local discontinuities which typically play a fundamental role in the behaviour of granular materials. This discontinuous nature induces special features such as anisotropy or local instabilities, which are difficult to understand or model based on the principles of continuum mechanics [6].

The Discrete Element Method (DEM) is an alternative approach that considers the granular nature of the material and provides a new insight in the constitutive model, being, nowadays, one of the most powerful and efficient tools to reproduce the behaviour of bulk materials [6]. Within the DEM approach, presented by Cundall and Strack [7] in 1979, each material grain is simulated as a rigid particle. The deformation of the material is represented by the interaction between the particles, allowing small overlaps. The normal and tangential contact between the rigid particles define the material constitutive behaviour.

DEM has proven to be a very useful tool to obtain complete qualitative information on calculations of groups of particles [6]. However, the computational cost of contact detection between Discrete Elements (DEs) is high and limits the applicability of the method to some practical problems, where millions of particles are typically involved. This problem is especially relevant when non-spherical particles are employed. This limitation, together with the uncertainty about the real contact mechanics and particle properties influencing the global behaviour of bulk materials [8], has led to different particle shape simplifications [9]:

- **Rolling friction** refers to an additional torque (rolling resistance torque) that is applied to each particle pair in contact and resists the rolling motion. This approach is typically applied to spherical DEs. Its main advantage is the low computational cost, since only the radii and the position of the centre of the spheric particles are required for the contact detection. Contact force calculation between spherical DEs is also straightforward, as the direction of the normal force is that of the vector that joins the spheres centres.
- **Sphere clusters** approach consists of representing each DE particle as a group of overlapping spheres joined rigidly, thereby allowing the use of algorithms that are straightforward extensions of the efficient methods used for spheres. This approach was used to represent geomaterials [10–14] with non-

* Corresponding author.

E-mail address: jirazabal@cimne.upc.edu (J. Irazábal).

spherical particles. The total amount of spheres in the model is $n \times p$, where n is the number of spheres per cluster, and p is the number of particles to be considered in the model. The necessary value of n to properly represent the roughness of a typical sand grain in 3D ranges from 100 to 400. In engineering calculations, where only macroscopic results are searched for, particles with 10–20 spheres can be appropriate [15]. In both cases, there is a relevant increase of contact detection time.

It should also be noted that this approach introduces geometric friction due to the undesired cavities between overlapped spheres.

Traditionally, the contact detection is split into two stages: Global Neighbour Search (GNS) and Local Contact Resolution (LCR). Although both stages can be optimised [16–18], the computational time grows at least proportionally to the increase in the total amount of spheres in the model.

- **Superquadrics** are a family of geometric shapes defined by formulas that resemble those of ellipsoids and other quadrics, except that the squaring operations are replaced by arbitrary powers. Contact calculation between two superquadrics was addressed by different authors in the last ten years [19–21].

Although superquadrics are a promising option to represent granular materials with the DEM, the computational cost of contact detection is high. Podlozhnyuk and Kloss [22] reported that the computational cost for superquadrics was 35 times higher than for spheres, in a simulation with 4860 DEs.

- **Polyhedral** particles representation allows the use of sharp edges and corners, which can be useful to reproduce many kinds of granular material particles. However, this approach leads to an increase of GNS and LCR computational time.

An extensive effort was made to use polyhedral particle shapes. Cundall et al. [23,24] developed a technique to detect contact forces between polyhedrons called the common plane method. It is a computationally expensive iterative method that replaces the contact between two polyhedrons with two plane-polyhedron contacts. This method was further improved by fast determination of the common plane [25]. Elias [26] presented a new method of estimating the contact force between two polyhedrons based on calculating the intersecting volume, and applied it to the calculation of railway ballast behaviour. Although the results obtained were promising, the simulations involved only 120 particles, due to computational time issues. Aiming to improve contact detection and force evaluation, Alonso-Marroquín and Wang [27,28] developed the spheropolygons approach in 2D. It is based in sweeping a sphere around a polygon, which leads to an easier force evaluation, and a decrease in LCR computational time. Galindo-Torres and Pedroso [29] extended it to more complex interactions in 3D, resulting in the spheropolyhedrons approach, which was used to predict granular materials behaviour [30].

Ahmed et al. [21] presented a new algorithm called the potential particle shapes approach. It is based in representing the particles as adjustably rounded polyhedrons. The limitation of this approach is that it is only able to represent convex particles.

In summary, the computational time of sphere cluster calculations augments proportionally to the increase of the amount of spheres in the model. For superquadrics, polyhedrons, spheropolyhedrons and potential particles, it strongly depends on the number of DEs and contacts, but the published works [22,21,26,31] are limited to a few thousands of particles.

In this work, rolling friction simplification was chosen due to its simplicity and lower computational requirements.

The paper starts with the introduction of the basic formulation of the DE model used. Next, the new insight for the application of the rolling resistance torque, called the Bounded Rolling Friction

(BROF) model, is presented, including some validation tests. Finally, the proposed method is used to reproduce a laboratory test that evaluates the lateral resistance of a ballast layer.

2. Model formulation

2.1. Basic features

2.1.1. Force evaluation

The behaviour of granular materials is governed by grain-grain contact interactions. This is the basis of the DEM approach, where the material is characterised by means of defining the interactions between its constituent particles. In the basic DEM formulation, standard rigid body dynamics equations define the translational and rotational motion of particles. For the i th particle, these equations can be written as

$$m_i \ddot{\mathbf{u}}_i = \mathbf{F}_i \tag{1}$$

$$\mathbf{I}_i \dot{\boldsymbol{\omega}}_i = \mathbf{T}_i \tag{2}$$

where $\ddot{\mathbf{u}}_i$ is the particle centroid acceleration in a fixed coordinate system \mathbf{X} , $\dot{\boldsymbol{\omega}}_i$ is the angular acceleration, m_i is the particle mass, \mathbf{I}_i is the second order inertia tensor with respect to the particle centre of mass, \mathbf{F}_i is the resultant force, and \mathbf{T}_i is the resultant moment about the central axes. \mathbf{F}_i and \mathbf{T}_i are computed as the sum of: (i) all forces and moments applied to the i th particle due to external loads, \mathbf{F}_i^{ext} and \mathbf{T}_i^{ext} , respectively, (ii) contact interaction forces, \mathbf{F}^{ij} , where j is the index of the neighbouring particle ranging from 1 to the number of elements n_i^c in contact with the particle under consideration i and (iii) all forces, \mathbf{F}_i^{damp} , and moments, \mathbf{T}_i^{damp} , resulting from external damping. \mathbf{F}_i and \mathbf{T}_i can be expressed as

$$\mathbf{F}_i = \mathbf{F}_i^{ext} + \sum_{j=1}^{n_i^c} \mathbf{F}^{ij} + \mathbf{F}_i^{damp} \tag{3}$$

$$\mathbf{T}_i = \mathbf{T}_i^{ext} + \sum_{j=1}^{n_i^c} \mathbf{r}_c^{ij} \times \mathbf{F}^{ij} + \mathbf{T}_i^{damp} \tag{4}$$

where \mathbf{r}_c^{ij} is the vector connecting the centre of mass of the i th particle and the contact point c with the j th particle (Fig. 1(a)).

The contact between the two interacting spheres can be represented by the contact forces \mathbf{F}^{ij} and \mathbf{F}^{ji} (Fig. 1(a)), which satisfy $\mathbf{F}^{ij} = -\mathbf{F}^{ji}$. Each force \mathbf{F}^{ij} is decomposed into the normal and tangential components, \mathbf{F}_n^{ij} and \mathbf{F}_t^{ij} , respectively (Fig. 1(b))

$$\mathbf{F}^{ij} = \mathbf{F}_n^{ij} + \mathbf{F}_t^{ij} = F_n \mathbf{n}^{ij} + \mathbf{F}_t^{ij} \tag{5}$$

where \mathbf{n}^{ij} is the unit vector normal to the contact surface at the contact point.

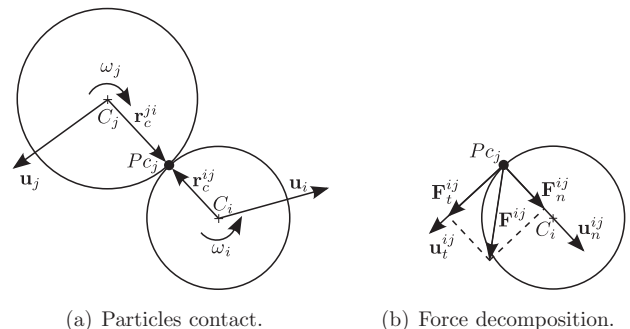


Fig. 1. Decomposition of the contact force into normal and tangential components [32].

The tangential force \mathbf{F}_t^{ij} , along the tangential direction \mathbf{t}^{ij} (Fig. 1 (b)), can be written as

$$\mathbf{F}_t^{ij} = F_{t_1} \mathbf{t}_1^{ij} + F_{t_2} \mathbf{t}_2^{ij} \quad (6)$$

where F_{t_1} and F_{t_2} are the tangential force components along the tangential directions \mathbf{t}_1 and \mathbf{t}_2 , respectively.

2.1.2. Constitutive model

The contact forces F_n, F_{t_1} and F_{t_2} are obtained using a constitutive model formulated for the contact between two DEs or a DE and a rigid facet. In the simulations carried out in this work, the classical Hertz-Midlin constitutive model along with viscous damping [33] was used for the contact evaluation, modified by introducing an additional material parameter called 'rolling friction coefficient'.

With respect to the detection of contact between DE spheres and rigid boundaries, the *Double Hierarchy Method* H^2 was followed [18]. To apply this algorithm, boundary surfaces should be discretised using triangle or quadrilateral meshes. A common binned data structure is used with the different types of objects (spherical DEs and triangular or quadrilateral elements) in order to efficiently search for potential neighbours. The contact search algorithm is particularised a posteriori for each distinct type of contact, i.e., particle-face, particle-edge etc., in order to establish pair-wise contacts at each time step.

2.1.3. Time integration

Eqs. (1) and (2) are integrated in time using a simple Central-Differences scheme [34].

Explicit integration in time yields high computational efficiency and enables the solution of large models. On the contrary, it is conditionally stable, so the magnitude of the time step Δt is limited [35]. The critical time step is determined by the highest natural frequency of the system.

2.2. Bounded Rolling Friction (BROF) model

Rolling friction calculation can be addressed by different formulations. Ai et al. [36] presented four different types:

- Models type A: the direction of the rolling resistance torque is always against the relative rotation between the two contacting entities, and its magnitude depends on the material properties and the contact normal force [37].
- Models type B: the magnitude of the rolling resistance torque depends on the angular velocity [37]. There are some situations where these models do not predict rolling friction when it is required, due to its dependence on surface velocity difference between two particles. In these cases, they are highly inaccurate.
- Models type C: the rolling resistance torque is the sum of a mechanical spring torque and a viscous damping torque [38]. In dynamic situations, models A and C (without damping) should converge to the same behaviour. Ai et al. [36] showed that model C is superior in static situations.
- Models type D: the rolling resistance torque depends on the total rotation or rotational velocity of a particle [39]. These models are clearly inefficient [36].

Models B and D will not be further commented in this paper due to their limitations.

A and C are the most commonly used rolling friction model types [8]. In this work, model A was improved to avoid the inconsistencies appearing in static situations. The main advantage of model A over model C is that only one parameter is required to completely define each material rolling friction.

In model type A the rolling resistance torque \mathbf{T}^r is given by

$$\mathbf{T}^r = -e^c |\mathbf{F}^n| \frac{\boldsymbol{\omega}^{rel}}{|\boldsymbol{\omega}^{rel}|} \quad (7)$$

where e^c is the resistance parameter that defines the contact rolling friction, which depends on the size and material properties of the particles in contact. \mathbf{F}^n is the normal contact force and $\boldsymbol{\omega}^{rel}$ is the relative angular velocity of the two particles in contact. Fig. 2 shows schematically the implementation of the rolling friction model type A.

The material property that influences the rolling behaviour of the DE particles is called rolling friction coefficient (η_r), which depends on the shape of the granular material particles: it will be higher for sharp stones than for pseudo-spherical ones. The rolling resistance parameter, e^c , depends on the rolling friction coefficient (η_r) and the radius of both contacting spheres.

Till this point, e^c was treated as the rolling resistance parameter. However, it can also be defined as the eccentricity of the contact. The need of this parameter is based on the fact that, when dealing with non-spherical particles contact, the line of action of the contact normal force does not pass through the centroid of the particles [8]. In the classical model A, the rolling resistance parameter for particle i (e_i^c) is considered as the product of its rolling friction coefficient $\eta_{r,i}$ and the effective rolling radius R^r [8,36], which, for two particles i and j in contact, is calculated as

$$\mathbf{R}^{r,ij} = \frac{r_i r_j}{r_i + r_j} \quad (8)$$

In the BROF model $e^c = \min(\eta_i |\mathbf{r}_i|, \eta_j |\mathbf{r}_j|)$. This allows a more realistic consideration of the contact between particles with very different radius sizes, because the eccentricity of the contact is defined by the lowest eccentricity of the contacting particles. This feature can be clearly noticed in the scheme of Fig. 3.

Ai et al. [36] outlined that model A should be used with caution in static situations, because rapid oscillations in the rolling resistance torque can appear due to the discontinuity in Eq. (7) at $|\boldsymbol{\omega}^{rel}| = 0$. To avoid this drawback, the BROF model limits the rolling resistance torque (\mathbf{T}_i^r) to the necessary moment to stop the sphere rotation in one time step (\mathbf{T}_i^{max})

$$\mathbf{T}_i^{max} = \boldsymbol{\omega}_i \mathbf{I}_i \Delta t - \sum_{j=1}^{n_c} \mathbf{r}_c^{ij} \mathbf{F}_c^{ij} \quad (9)$$

$$\text{if } \|\mathbf{T}_i^r\| < \|\mathbf{T}_i^{max}\| \rightarrow \mathbf{T}_i^r = -e^c |\mathbf{F}^n| \frac{\mathbf{T}_i^{max}}{\|\mathbf{T}_i^{max}\|}$$

$$\text{if } \|\mathbf{T}_i^r\| \geq \|\mathbf{T}_i^{max}\| \rightarrow \mathbf{T}_i^r = \mathbf{T}_i^{max}$$

where $\boldsymbol{\omega}_i$ is the angular velocity of the sphere i in the previous time step.

It should be noted that, within the BROF model, the rolling resistance torque is applied in the direction of the necessary moment to stop the sphere rotation in one time step (\mathbf{T}_i^{max}), and not in the direction of the relative angular velocity of the two par-

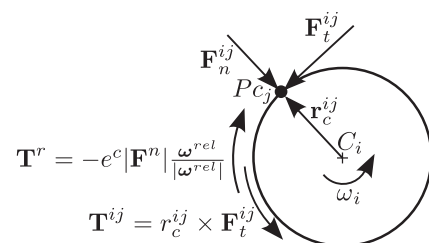


Fig. 2. Scheme of rolling resistance model type A.

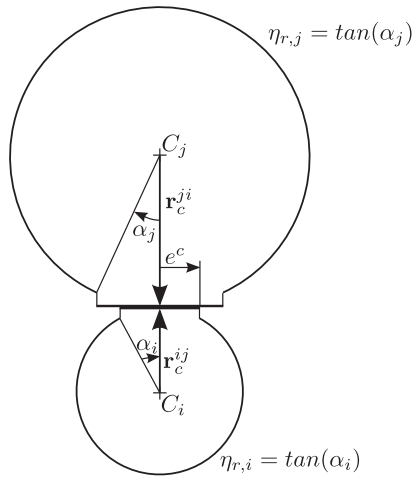


Fig. 3. Schematic representation of the effect of the rolling friction parameters e^c and η_r .

ticles in contact ($|\omega^{rel}|$). This was set in order to avoid discrepancies, making the algorithm frame-independent.

Eq. (10) highlights the differences in the computation of the rolling resistance torque between the classical model A and the BROF model.

$$\begin{aligned} \text{Model type A} \quad \mathbf{T}_i^r &= -e^c |\mathbf{F}^n| \frac{\omega^{rel}}{|\omega^{rel}|} \\ \text{BROF model} \quad \mathbf{T}_i^r &= -e^c |\mathbf{F}^n| \frac{\mathbf{T}_i^{max}}{|\mathbf{T}_i^{max}|} \end{aligned} \quad (10)$$

This improvement, based on the work of Tasora and Anitescu [40], avoids undesirable oscillations in the spheres spin.

2.3. Software

The data structures and algorithms have all been implemented through the *Kratos multiphysics* software suite [41], an Open-Source framework for the development of numerical methods for solving multidisciplinary engineering problems. Within *Kratos multiphysics*, a DEM code called *DEMPack* (www.cimne.com/dem-pack/) was implemented.

3. BROF model validation

Two of the benchmark cases described by Ai et al. [36] were selected for the validation of the BROF model. In both cases, the same material properties and simulation parameters described in [36] were used.

3.1. Test case 1: sphere with initial velocity rotating over a flat surface [36]

The first test adopted is a single sphere (with rolling friction) rotating over a flat surface. To develop the simulation, a sphere is placed over a rigid surface letting it move by its own weight until it achieves equilibrium. Then, an initial translational velocity ($v_0 = 1.0 \text{ m/s}$) is applied to the sphere. The test case layout is shown in Fig. 4.

The material properties and simulation parameters used in test cases 1 and 2 are summarised in Table 1.

Fig. 5 shows the rolling resistance torque over time using the BROF model, as compared to that obtained with the classic rolling friction model type A [36]. In the dynamic part of the simulation, the rolling resistance torque in both models is a constant value given by Eq. (7).

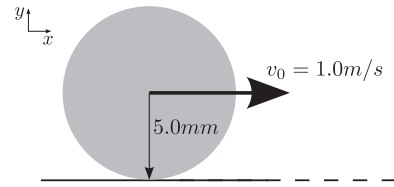


Fig. 4. Initial layout of test case 1.

Table 1

Material properties and calculation parameters used in test cases 1 and 2.

Material properties	
Density (kg/m^3)	1056
Young modulus (Pa)	$4.0 \cdot 10^7$
Poisson ratio	0.49
Restitution coefficient	0.2
Friction coefficient DE/FE	0.8
Rolling friction coefficient	0.2
Calculation parameters	
Gravity (m/s^2)	-9.8
Time step (s)	$5.0 \cdot 10^{-5}$
Neighbour search frequency	10

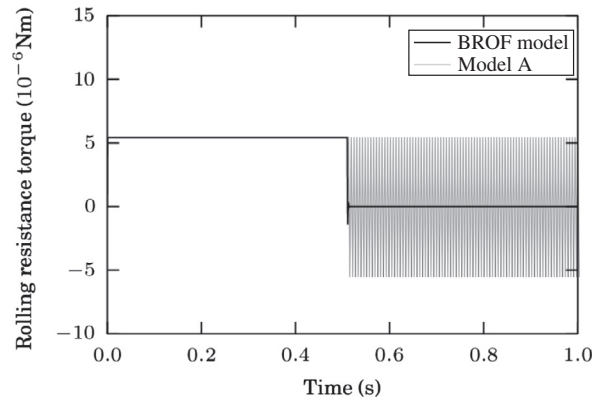


Fig. 5. Comparison between rolling resistance torque obtained applying the classic rolling friction model A and the BROF model.

However, once the sphere reaches its final position, differences between both models arise. In the classic model A, the torque oscillates between a positive and a negative value with the same magnitude. The BROF model overcomes this inconvenience thanks to the limitation imposed in Eq. (9), and leads to an equilibrium situation where the rolling resistance torque and the particle angular velocity are zero.

The torque instability for model A generates oscillations in angular velocity, which are also eliminated with the BROF model. Although their magnitude is low for the test case 1, the kinetic energy generated can be relevant in simulations involving a large amount of particles.

With model C, damping is necessary to avoid oscillations in a static situation. Without damping, the behaviour would be similar to the behaviour of model A, but the oscillating frequency does not depend on the step: it depends on the rolling stiffness and the mass of the sphere.

The graph in Fig. 6 shows the response of the BROF model and the classic rolling friction model C with a damping ratio $\delta_r = 0.3$. It can be appreciated that, in model C, some oscillations still appear although damping is applied. The amplitude of the oscillation decreases gradually with time.

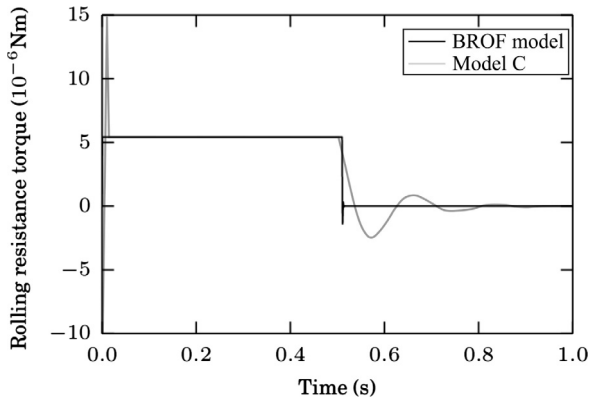


Fig. 6. Comparison between rolling resistance torque obtained applying the classic rolling friction model C with a damping ratio $\delta_r = 0.3$ and the BROF model.

The results obtained for test case 1 show that BROF model outperforms models A and C. The difference is less relevant for model C.

3.2. Test case 2: sphere with initial angular velocity rotating over an inclined surface [36]

The aim of the second test case is to evaluate the influence of varying the rolling friction coefficient in the BROF model. It consists of a sphere rolling up a slope with an angle of $\beta = 10$ degrees, as shown in Fig. 7. The sphere has the same properties as in test case 1 (see Table 1). In this case the sphere is positioned over the rigid surface allowing it to move by its own weight, but restringing its movement in the x direction (see Fig. 7). When the sphere come to rest, x movement restriction is removed and an initial translational velocity $v_0 = 1.0$ m/s, parallel to the slope, is applied.

In order to evaluate the influence of the rolling friction coefficient in the sphere response, two other values of the rolling friction coefficient η_r were considered. When η_r is lower than 0.176 (which corresponds to a rolling friction angle $\alpha = 10$ degrees) the sphere should roll back downwards after reaching its highest point. When η_r is sufficiently large (more than 0.176), the sphere should be stopped by a resistance torque that prevents the downward rolling due to gravity.

Fig. 8(a) shows the evolution of the rolling resistance torque over time. It is worth noting that applying the BROF model, the rolling resistance torque in dynamic situations is constant for a specific value of the rolling friction coefficient. However, when the particle comes to rest, the rolling resistance torque is set to a specific value, which is the necessary torque to stop the sphere rotation in one time step. This feature can be clearly appreciated in Fig. 8(a), for $\eta_r = 0.2$ and 0.4, where the rolling resistance torque is the same independently of the value of the rolling friction coefficient.

Fig. 8(b) shows the sphere rolling distance over time. It can be observed that, with a higher rolling friction coefficient, the sphere

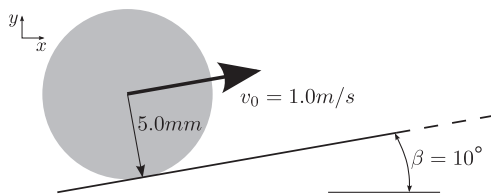
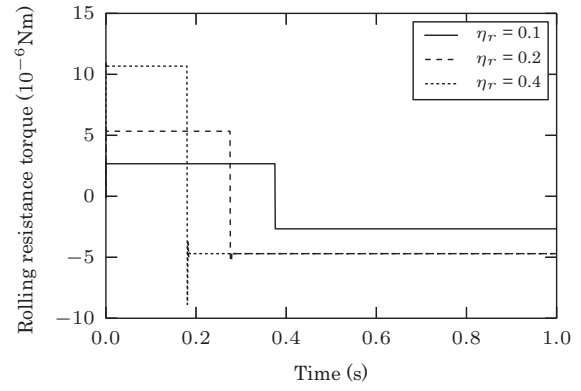
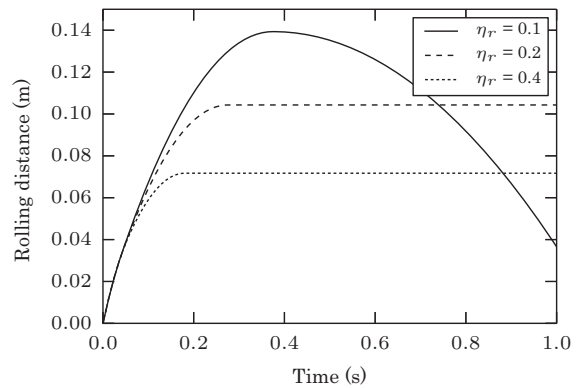


Fig. 7. Initial layout of test case 2.



(a) Rolling resistance torque versus time.



(b) Rolling distance versus time.

Fig. 8. Test case 2 results for three different rolling friction coefficients $\eta_r = 0.1, 0.2$ and 0.4 applying the BROF model.

spin stops faster. As expected, the sphere rolls back downwards after reaching its highest point for $\eta_r = 0.1$.

Fig. 9 presents the results obtained by Ai et al. [36] with the classic rolling friction model C with a damping ratio $\delta_r = 0.3$. Although the rolling resistance torque is similar, BROF model avoids oscillations with only one parameter to calibrate.

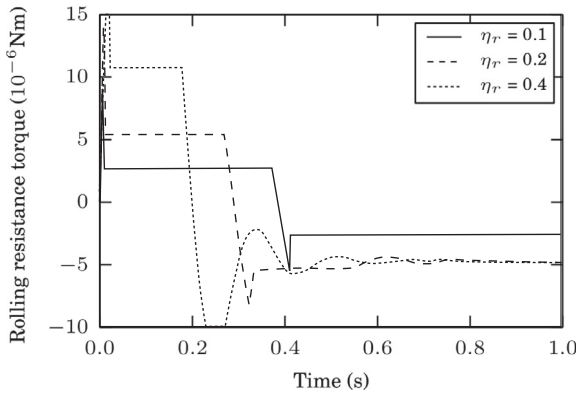
4. Railway ballast behaviour calculation

4.1. Ballast characterisation

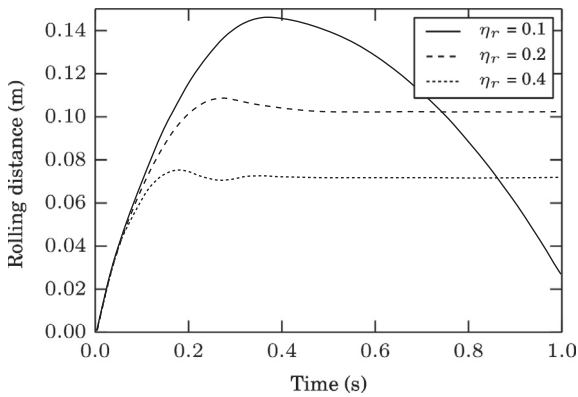
Railway ballast refers to the layer of crushed stones placed between and underneath the sleepers. The purpose of this layer of granular material is to provide drainage and structural support for the dynamic loading applied by trains [42].

The ballast layer is relatively inexpensive and easy to maintain. However, the demands over the ballasted track are increasing due to the faster, heavier and more frequent trains, which yields to the necessity of a better understanding of its mechanics and the way in which it resists lateral and vertical loads [21].

Mechanical testing on specimens of railway ballast is difficult to carry out in traditional laboratory devices owing to the large particle size [43]. Thus, there is interest in developing simulation techniques that enable the numerical analysis of the mechanical behaviour of ballast. Railway ballast is an ideal material to be calculated with the DEM [21], due to its granular nature and relatively large grain size, compared with the depth of the ballast layer.



(a) Rolling resistance torque versus time.



(b) Rolling distance versus time.

Fig. 9. Test case 2 results for three different rolling friction coefficients $\eta_r = 0.1, 0.2$ and 0.4 applying the classic rolling friction model C with a damping ratio $\delta_r = 0.3$ [36].

Some material properties of ballast are well documented in technical literature. In this work, the following values were adopted:

- Density: 2700 kg/m^3 [44].
- Particle size: ballast granulometry is regulated [45]. Following the indications of European standards, the mean diameter of the particles was set to 0.05 m .
- Poisson ratio: 0.18 [46,44].
- Restitution coefficient: 0.4 [46].
- Angle of repose: 40 degrees [13].

There is some scope for uncertainty in the choice of the Young modulus value. For real ballast stones, some authors suggest $E = 30 \text{ GPa}$ [47,48]. However, contacts between real ballast stones are not Hertzian, as the particles have rough and non-spherical surfaces [49]. For rough surfaces, the contact radius of curvature is much smaller than for idealised spherical shapes. As a consequence, the appropriate value of the Young modulus when using spheres is lower. Ahmed et al. [21] used values of shear modulus (G) between 1 and 10 GPa , that corresponds to a value of the Young modulus between 2.36 and 23.6 GPa for the chosen Poisson ratio ($\nu = 0.18$). In this work, we tested four values within that range: $E = 5.9, 11.8, 17.7$ and 23.6 GPa , which correspond to $G = 2.5, 5, 7.5$ and 10 GPa .

The friction coefficient between ballast stones depends on the time and the load cycles suffered by ballast stones. According to Melis [44], the friction angle should always be between 30 and

40 degrees (friction coefficient between 0.577 and 0.839). In this work, a value of 0.6 was selected, following Chen et al. [13].

As mentioned before, ballast particles were represented as spherical DEs with rolling friction. The value of the rolling friction coefficient was calibrated to reproduce the angle of repose of ballast, as described in the following section.

4.2. Angle of repose

The angle of repose is defined as the slope of a pile of granular material laid up on the ground without any other support [50]. The importance of this material property is that it controls all parameters that affect the behaviour of large amounts of granular material (friction between particles, shape and size of different grains), allowing their evaluation in a simple way.

Fig. 10 shows the layout of the simulation (taken from Chen et al. [13]) developed to calibrate the rolling friction coefficient of the material. The test is based on measuring the angle of repose for each of the rolling friction coefficients evaluated. In the simulation, particles are deposited from a hopper with a squared aperture of 25 cm side, located 0.7 m above the floor.

Material and calculation parameters are defined in Table 2. The critical time step of the system is determined by its highest natural frequency, and depends on the mass and the stiffness of the particles. For that reason, different time steps were used for each simulation.

Fig. 11 shows the angle of repose obtained for each value of the rolling friction coefficient. It corresponds to the tests for $E = 17.7 \text{ GPa}$, though the results were independent of the Young modulus (results not shown).

Since the angle of repose of ballast is 40 degrees, the rolling friction coefficient was set to 0.25 for the benchmark test described in the following section.

It should be noted that the rolling friction approach can be useful to reproduce other granular materials with spherical DEs.

4.3. Ballast layer lateral resistance

One of the problems that may appear in railway infrastructures is lateral buckling, which is one of the most critical troubles in railroad tracks [51]. It can greatly affect the circulation and may cause catastrophic derailments [52]. Lateral buckling can be caused by mechanical or thermal loads, being relatively common in countries with large deviations in temperature between winter and summer.

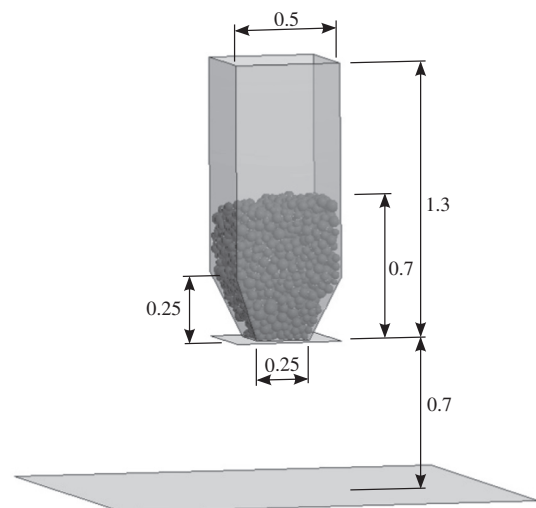


Fig. 10. Simulation layout (measurements in metres) [13].

Table 2

Data summary.

Material properties	
Density (kg/m ³)	2700
Poisson coefficient	0.18
Young modulus (GPa)	5.9/11.8/17.7/23.6
Friction coefficient	0.6
Restitution coefficient	0.4
Rolling friction coefficient	0.2/0.25/0.3
Calculation parameters	
Time step (μs)	8.0/6.0/5.0/4.0
Neighbour search frequency	10

For this reason, lateral resistance of the track is one of the most important parameters regarding track stability. In this context, the ballast plays a crucial role [51].

Because of the importance of this problem, we developed a numerical simulation to evaluate the lateral resistance force of a ballast layer against a sleeper with imposed motion.

A reference experimental test [53] was reproduced numerically, and the results were compared.

4.3.1. Reference test

Zand and Moraal [53] conducted a series of three-dimensional ballast resistance tests using a rail track panel. Those tests were performed in the Roads and Railways Research Laboratory of the Delft University of Technology (TU Delft).

The tests consisted of a track panel with five sleepers inside a ballast bed (Fig. 12). Lateral load was applied by means of two diagonal rods connecting the hydraulic actuator (150 kN) to the track section. Two connecting beams were welded between the rails to reinforce the track panel enabling a more uniform load application. The motion of the track panel was imposed and the opposing force was measured.

The laboratory tests were performed for different vertical loads. In this work, the test with unloaded sleepers was chosen for the numerical calculation.

4.3.2. DE model

The geometry used in the simulations is the same as in the laboratory test, but for only one sleeper, instead of five (see Fig. 13). Lateral resistance test simulations were developed using spherical discrete elements with rolling friction.

Particles initial distribution is a key parameter that has not been already mentioned, since it is specific for numerical modelling, though irrelevant for the case described in Section 4.3.1.

To start the calculation, the volume has to be filled with spherical DEs. Although there exist sphere meshers (e.g. GiD pre and post-processor sphere mesher, <http://www.gidhome.com/>), the result do not always meet the desired material compactness. As a result, new alternatives need to be considered to address the problem.

Tran [54] proposed the so-called gravitational packing technique to generate DE samples for granular material simulations. It consists in assigning the particles a zero friction coefficient value, and letting them to freely fill the volume under consideration. This

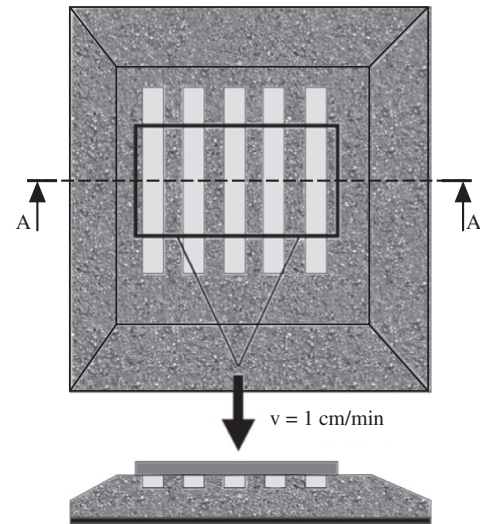


Fig. 12. Laboratory test layout [53].

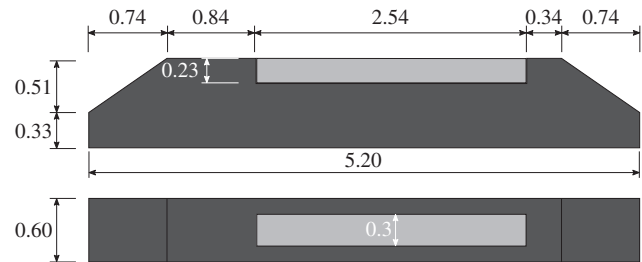


Fig. 13. Test geometry for calculating ballast lateral resistance force against sleeper movement (distances in metres).

leads to a high particle compactness, though requires a pre-simulation. This is the method applied in this work.

In this specific case, an auxiliary surface is needed to maintain the slope of the embankment when the material friction angle is zero.

Fig. 14 shows the layout of the numerical model at the beginning and at the end (time = 2.5 s) of the pre-simulation. The auxiliary surfaces move downwards together with the granular material in order to maintain the desired geometry. In Fig. 14 it can also be seen that an auxiliary sleeper, higher than the real one, was used to keep the geometry of the ballast layer.

At the end of the pre-simulation, it was verified that the value of the vertical force on the upper part of the auxiliary surfaces was zero (otherwise, the ballast layer would be over-compacted).

The particle arrangement at the end of the pre-simulation was the starting point of the laboratory test numerical calculation. The DE mesh, consisting of 21,708 spheres, is shown in Fig. 15.

The friction between ballast and the outer walls was considered null to simulate a continuous domain with mirrored particles. Hence, the results of the numerical model can be compared to

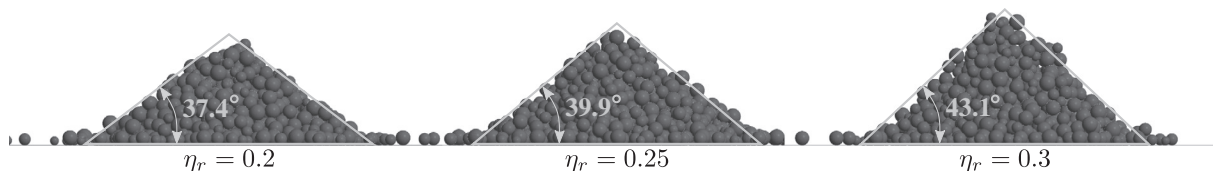


Fig. 11. Repose angle of the granular material for different rolling friction parameters ($E = 17.7$ GPa).

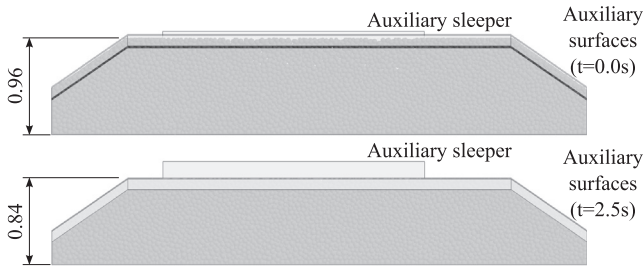


Fig. 14. Auxiliary surfaces used to keep the geometry during the pre-simulation.

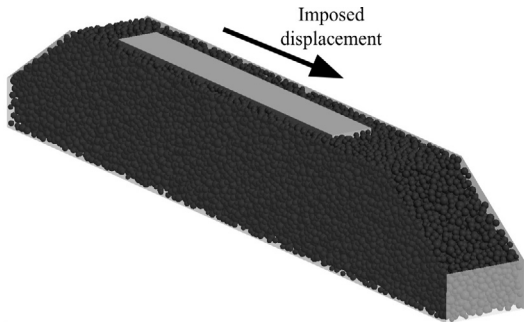


Fig. 15. Initial configuration for the ballast resistance numerical test.

those obtained in the experiment, where the lateral force was applied to 5 sleepers.

The material properties and calculation parameters were defined in Table 2. The rolling friction coefficient was set to 0.25, based on the results of Section 4.2. The value of the friction coefficient between the ballast stones and the sleeper was taken from the reference study [53], where it was computed experimentally.

4.3.3. Results

Fig. 16 shows the results of the lateral resistance force versus the sleeper displacement. The numerical and the experimental results are compared.

It can be observed that the results in the first loading stages for $E = 17.7$ GPa and $E = 23.6$ GPa are almost identical, and close to the experimental curve. For lower values of E , the slope is also lower. The differences in terms of the maximum resistance force are less relevant, with certain erratic behaviour.

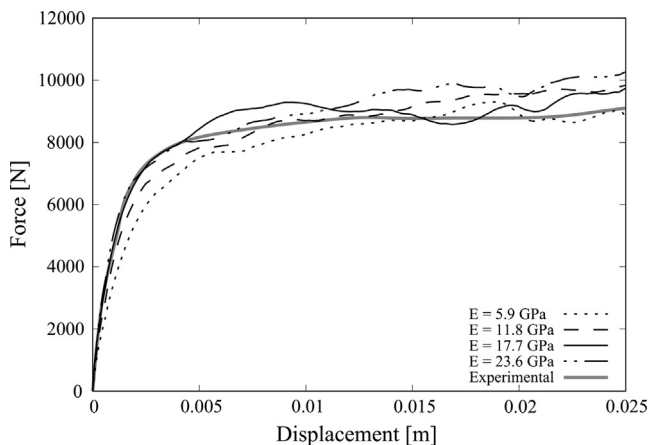


Fig. 16. Numerical results of the ballast resistance test for four different values of the Young modulus, and comparison to the experimental test.

These results suggest that for this test, the influence of E is negligible provided that some value greater than 17.7 GPa is chosen. Since lower values allow for larger time steps and low computational time, it is advantageous to use $E = 17.7$ GPa.

An interesting feature of the numerical methods is that they allow obtaining results difficult to measure in experimental facilities. As an example, the percentage of the lateral resistance force exerted by ballast against each face of the sleeper can be computed. This information can be useful to optimise the geometry of the cross-section to increase the lateral resistance force under different situations.

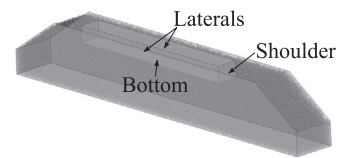
Fig. 17 shows the results. It can be seen that at the start of the simulation, 50% of the resisting force is due to the friction of the bottom face. However, that percentage decays sharply up to 20% for displacement equal to 3 mm, while it grows for the shoulder, whose force is higher for displacement greater than 1 mm.

According to these results, the most effective way to increase the lateral resistance would be to augment the roughness of the bottom face of the sleeper. If lateral displacements greater than 1 mm were allowed, the geometry of the shoulder should be optimised.

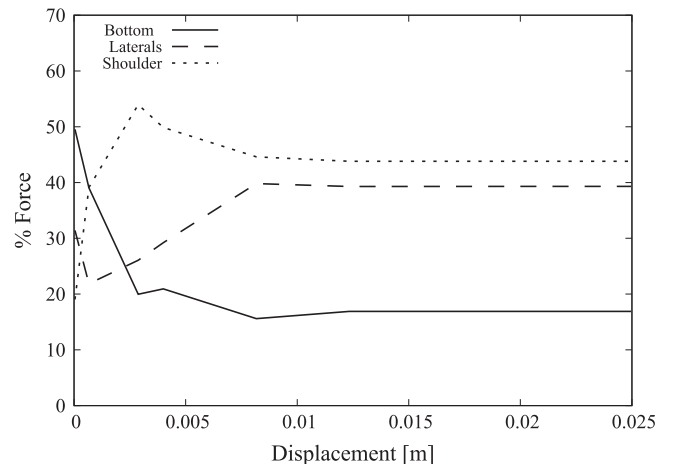
A more comprehensive analysis would be required to draw conclusions in a practical case, including the analysis of loaded scenarios.

5. Summary and conclusions

A new model, called the Bounded Rolling Friction (BROF), for the computation of rolling friction for spherical DE particles was presented. Besides providing similar results than the previous rolling friction models in dynamic situations, it includes a limitation to the angular velocity in order to avoid undesirable sphere rotation when the particle is almost at rest. The BROF model was compared with previous rolling friction models, concluding that the results are accurate, with only one parameter (η_r) to be calibrated. BROF model sensitivity to changes in η_r was also checked.



(a) Sleeper faces.



(b) Percentage of the lateral resistance force.

Fig. 17. Percentage of the lateral resistance force acting on each sleeper face.

It can be concluded that the BROF model outperforms previous approaches for modelling irregular particle shapes with spherical DEs.

To calibrate the BROF model η_r parameter, the angle of repose of the granular material can be used, since it is easy to obtain it in the laboratory. In the case study presented, an angle of repose of 40 degrees was obtained for ballast with $\eta_r = 0.25$.

The BROF model with spherical DEs was used to reproduce an experimental test on the lateral resistance of ballast against a sleeper with imposed motion. The initial stiffness was correctly reproduced, and the maximum force was captured with an error of almost the 6%.

DEM allows detailed analyses of the system response, which are often difficult to carry out in laboratory. In the benchmark presented, the evolution of the relative influence in the resistant force of each component of the ballast layer was identified.

The results showed some degree of dependence on the Young modulus value. In particular, they suggest that a minimum value of 17.7 GPa (correspondent to a shear modulus of 7.5 GPa) should be considered. Hence, calibration of this parameter seems advisable before applying this model to reproduce ballast behaviour under different load conditions.

Although the results suggest that spherical DEs can be appropriate to reproduce the macroscopical behaviour of large domains featuring a high amount of particles (as is the case of the ballast bed), it is obvious that a more accurate description could be achieved with more realistic particle shapes. The authors are currently working in this line by using clusters of spheres.

Acknowledgements

This work was carried out with the financial support Spanish MINECO within the BALAMED (BIA2012-39172) and MONICAB (BIA2015-67263-R) projects.

We appreciate the reviewers the time taken to provide valuable comments that have improved undoubtedly the quality of the article.

References

- [1] Duncan J. State of the art: limit equilibrium and finite-element analysis of slopes. *J Geotech Eng-ASCE* 1996;122(7):577–96.
- [2] Dafalias Y, Manzari M. A critical state two-surface plasticity model for sands. *Géotechnique* 1997;47(2):255–72.
- [3] Indraratna B, Nimbalkar S, Coop M, Sloan SW. A constitutive model for coal-fouled ballast capturing the effects of particle degradation. *Comput Geotech* 2014;61:96–107.
- [4] Esmaili M, Khodaverdian A, Neyestanaki HK, Nazari S. Investigating the effect of nailed sleepers on increasing the lateral resistance of ballasted track. *Comput Geotech* 2016;71:1–11.
- [5] Salazar F, Irazábal J, Larese A, Oñate E. Numerical modelling of landslide-generated waves with the particle finite element method (PFEM) and a non-Newtonian flow model. *Int J Numer Anal Met* 2015;40(6):809–26.
- [6] Belheine N, Plassiard J, Donzé F, Darve F, Seridi A. Numerical simulation of drained triaxial test using 3D discrete element modeling. *Comput Geotech* 2009;36(1–2):320–31.
- [7] Cundall P, Strack O. A discrete numerical model for granular assemblies. *Géotechnique* 1979;29(1):47–65.
- [8] Wensrich CM, Katterfeld A. Rolling friction as a technique for modelling particle shape in DEM. *Powder Technol* 2012;217:409–17.
- [9] Lane JE, Metzger PT, Wilkinson RA. A review of Discrete Element Method (DEM) particle shapes and size distributions for lunar soil. *Tech. rep., NASA*; 2010.
- [10] Matsushima T, Katagiri J, Uesugi K, Tsuchiyama A, Nakano T. 3D shape characterization and image-based DEM simulation of the lunar soil simulant FJS-1. *J Aerospace Eng* 2009;22:1(15):15–23.
- [11] Garcia X, Xiang J, Latham J-P, Harrison J-P. A clustered overlapping sphere algorithm to represent real particles in discrete element modelling. *Géotechnique* 2009;59(9):779–84.
- [12] Ferrellec J-F, McDowell GR. A method to model realistic particle shape and inertia in DEM. *Granul Matter* 2010;12(5):459–67.
- [13] Chen C, McDowell GR, Thom NH. Investigating geogrid-reinforced ballast: experimental pull-out tests and discrete element modelling. *Soils Found* 2014;54(1):1–11.
- [14] Ngo NT, Indraratna B, Rujikiatkamjorn C. DEM simulation of the behaviour of geogrid stabilised ballast fouled with coal. *Comput Geotech* 2014;55:224–31.
- [15] Indraratna B, Ngo NT, Rujikiatkamjorn C, Vinod JS. Behavior of fresh and fouled railway ballast subjected to direct shear testing: discrete element simulation. *Int J Geomech* 2014;14(1):34–44.
- [16] Han K, Feng Y, Owen D. Performance comparisons of tree-based and cell-based contact detection algorithms. *Eng Comput* 2007;24(2):165–81.
- [17] Horner DA, Peters JF, Carrillo A. Large scale discrete element modeling of vehicle-soil interaction. *J Eng Mech-ASCE* 2001;127(10):1027–32.
- [18] Santasusana M, Irazábal J, Oñate E, Carbonell JM. The double hierarchy method. A parallel 3D contact method for the interaction of spherical particles with rigid FE boundaries using the DEM. *Comp Part Mech* 2016;3(3):407–28.
- [19] Chakraborty N, Peng J, Akella S, Mitchell JE. Proximity queries between convex objects: an interior point approach for implicit surfaces. *IEEE Trans Robot* 2008;24(1):211–20.
- [20] Lopes DS, Silva MT, Ambrósio JA, Flores P. A mathematical framework for rigid contact detection between quadric and superquadric surfaces. *Multibody Syst Dyn* 2010;24(3):255–80.
- [21] Ahmed S, Harkness J, Le Pen L, Powrie W, Zervos A. Numerical modelling of railway ballast at the particle scale. *Int J Numer Anal Met* 2015;40(5):713–37.
- [22] Podlozhnyuk A, Kloss C. A contact detection method between two convex super-quadric particles based on an interior point algorithm in the discrete element method. In: *IV International Conference on Particle-Based Methods, Barcelona*.
- [23] Cundall PA. Formulation of a three-dimensional distinct element model-Part I. A scheme to detect and represent contacts in a system composed of many polyhedral blocks. *Int J Rock Mech Min* 1988;25(3):107–16.
- [24] Hart R, Cundall PA, Lemos J. Formulation of a three-dimensional distinct element model-Part II. Mechanical calculations for motion and interaction of a system composed of many polyhedral blocks. *Int J Rock Mech Min* 1988;25(3):117–25.
- [25] Nezami EG, Hashash YMA, Zhao D, Ghaboussi J. Shortest link method for contact detection in discrete element method. *Int J Numer Anal Meth Geomech* 2006;30(8):783–801.
- [26] Eliáš J. Simulation of railway ballast using crushable polyhedral particles. *Powder Technol* 2014;264:458–65.
- [27] Alonso-Marroquín F. Spheropolygons: A new method to simulate conservative and dissipative interactions between 2D complex-shaped rigid bodies. *EPL* 2008;83(1):14001.
- [28] Alonso-Marroquín F, Wang Y. An efficient algorithm for granular dynamics simulations with complex-shaped objects. *Granul Matter* 2009;11(5):317–29.
- [29] Galindo-Torres SA, Pedrosa DM. Molecular dynamics simulations of complex-shaped particles using Voronoi-based spheropolyhedra. *Phys Rev E* 2010;81(6):061303.
- [30] Richefeu V, Mollon G, Daudon D, Villard P. Dissipative contacts and realistic block shapes for modeling rock avalanches. *Eng Geol* 2012;149–150:78–92.
- [31] Ouhbi N, Voivret C, Perrin G, Roux J-N. Railway ballast: grain shape characterization to study its influence on the mechanical behaviour. *Proc Eng* 2016;143:1120–7.
- [32] Oñate E, Rojek J. Combination of discrete element and finite element method for analysis of geomechanics problems. *Comput Meth Appl Math* 2004;193:3087–128.
- [33] Casas G, Mukherjee D, Celigueta MA, Zohdi TI, Onate E. A modular, partitioned, discrete element framework for industrial grain distribution systems with rotating machinery. *Comp Part Mech* 2015;1:1–18.
- [34] Oñate E, Zárate F, Miquel J, Santasusana M, Celigueta MA, Arrufat F, et al. A local constitutive model for the discrete element method. application to geomaterials and concrete. *Comp Part Mech* 2015;2(2):139–60.
- [35] Zienkiewicz O, Taylor R, Fox D. *The finite element method for solid and structural mechanics*. 7th ed. Oxford: Butterworth-Heinemann; 2014.
- [36] Ai J, Chen J-F, Rotter JM, Ooi JY. Assessment of rolling resistance models in discrete element simulations. *Powder Technol* 2011;206(3):269–82.
- [37] Zhou YC, Wright BD, Yang RY, Xu BH, Yu AB. Rolling friction in the dynamic simulation of sandpile formation. *Phys A: Stat Mech Appl* 1999;269(2–4):536–53.
- [38] Iwashita K, Oda M. Rolling resistance at contacts in simulation of shear band development by DEM. *J Eng Mech-ASCE* 1998;124(3):285–92.
- [39] Sakaguchi H, Ozaki E, Igarashi T. Plugging of the flow of granular materials during the discharge from a silo. *Int J Mod Phys B* 1993;07(09n10):1949–63.
- [40] Tasora A, Anitescu M. A complementarity-based rolling friction model for rigid contacts. *Meccanica* 2013;48(7):1643–59.
- [41] Davdand P, Rossi R, Oñate E. An object-oriented environment for developing finite element codes for multi-disciplinary applications. *Arch Comput Method Eng* 2010;17(3):253–97.
- [42] Tutumluier E, Qian Y, Hashash YMA, Ghaboussi J, Davis DD. Discrete element modelling of ballasted track deformation behaviour. *Int J Rail Transp* 2013;1(1–2):57–73.
- [43] Chen C, Indraratna B, McDowell G, Rujikiatkamjorn C. Discrete element modelling of lateral displacement of a granular assembly under cyclic loading. *Comput Geotech* 2015;69:474–84.
- [44] Melis Maynar M. Embankments and ballast in high speed rail. *Revista de Obras Publicas* 2006;153:7–26.
- [45] *Aggregates for railway ballast*. EN 13450:2015.
- [46] Farmer I. *Engineering properties of rocks*. Spon; 1968.
- [47] Howatson AM, Lund PG, Todd JD. *Engineering tables and data*. London, UK: Chapman and Hall; 1972.

- [48] Aikawa A. Dynamic characterisation of a ballast layer subject to traffic impact loads using three-dimensional sensing stones and a special sensing sleeper. *Constr Build Mater* 2015;92:23–30.
- [49] Harkness J, Zervos A, Pen LL, Aingaran S, Powrie W. Discrete element simulation of railway ballast: modelling cell pressure effects in triaxial tests. *Granular Matter* 2016;18(3):65.
- [50] Taylor DW. *Fundamentals of soil mechanics*. J. Wiley; 1948.
- [51] Kabo E. A numerical study of the lateral ballast resistance in railway tracks. *Proc Inst Mech Eng Part F: J Rail Rapid Transit* 2006;220(4):425–33.
- [52] Gallego J, Gómez-Rey D. A finite element solution for the lateral track buckling problem. Technical Report, TIFSA-RENFE Group; 2001.
- [53] Zand Jvt, Moraal J. Ballast resistance under three dimensional loading. Tech. rep. Delft University of Technology; 1997.
- [54] Tran VDH, Meguid MA, Chouinard LE. Discrete element and experimental investigations of the earth pressure distribution on cylindrical shafts. *Int J Geomech* 2014;14(1):80–91.